

Nucleon exchange properties of the $E/A = 8.5$ MeV $^{74}\text{Ge} + ^{165}\text{Ho}$ reaction

R. Płaneta,* K. Kwiatkowski, S. H. Zhou,[†] and V. E. Viola

Department of Chemistry and Indiana University Cyclotron Facility, Indiana University, Bloomington, Indiana 47405

H. Breuer

Department of Physics, University of Maryland, College Park, Maryland 20742

M. A. McMahan

Accelerator and Fusion Research Division, Lawrence Berkeley Laboratory, University of California, Berkeley, California 94720

W. Kehoe and A. C. Mignerey

Department of Chemistry, University of Maryland, College Park, Maryland 20742

(Received 8 June 1989; revised manuscript received 5 September 1989)

Mass and charge distributions have been measured for damped projectile-like fragments in the reaction $^{74}\text{Ge} + ^{165}\text{Ho}$ at 8.5 MeV per nucleon bombarding energy. Coincidences were measured between Z - and A -identified projectile-like fragments and angle-correlated heavy reaction partners in order to derive the primary mass distribution for projectile-like fragments. Centroids and variances of the primary and post-evaporative Z , N , and A distributions are presented. The evolution of the primary N and Z distributions as a function of energy loss is found to deviate from predictions of the nucleon exchange transport model.

I. INTRODUCTION

Statistical transport models have proven generally successful in accounting for many major features of damped (deep inelastic) collisions between heavy nuclei at near-barrier bombarding energies.¹⁻³ For example, the energy dissipation, angular focusing, and nuclide distribution properties of these binary reactions are qualitatively reproduced within the context of these models. During the past few years, improved experimental techniques have made it possible to subject the models to more rigorous tests. Simultaneous measurements of fragment charge and mass distributions have permitted examination of the evolution of the nucleon-exchange process as a function of dissipated energy during the existence of the dinuclear complex formed in damped reactions.⁴⁻¹⁰ Related studies have also revealed important insights into the question of excitation-energy partition between the primary fragments at the moment of scission.¹⁰⁻¹⁶

Direct comparison of model calculations with experimental data for damped reactions between heavy nuclei is generally obscured by the subsequent decay of the excited primary fragments following scission of the dinuclear complex.¹⁷ Thus, in order to reconcile the measured post-evaporative charge and mass yields with the primary distributions predicted by theory, significant corrections must be applied to account for modifications due to deexcitation. These corrections require both a knowledge of how the excitation energy is partitioned between the two primary fragments and the application of a reliable statistical-decay model to relate the primary and observed data. Several inclusive measurements have been

performed in which primary fragment Z and A distributions have been deduced by applying corrections for statistical decay to the post-evaporative yields.^{4,6-7,10} These studies contain a major uncertainty in that they require *a priori* assumptions concerning the excitation-energy distribution of the fragments at scission. Similar problems affect the reverse approach, i.e., comparison of data with theoretical predictions that have added statistical decay to the calculated primary product yields. This arises because the models do not yield information on the widths of the excitation-energy distributions and dependence on fragment mass. The results consistently indicate distinct discrepancies between the model calculations and the data, especially with regard to the magnitude and direction of net proton and neutron transfer in these reactions.⁷

In order to reduce uncertainties in the determination of the primary nuclide distributions, we have performed a kinematic-coincidence measurement between damped projectile-like and target-like fragments, which permits determination of both the primary and post-evaporative fragment mass distributions over a large range of energy dissipation. These results can then be compared directly with nucleon exchange transport model calculations.¹⁻³ Furthermore, these data permit examination of several important questions concerning the partition of excitation energy in damped reactions,¹⁰⁻¹⁶ a subject that is addressed in the following paper.¹⁸

The experiment reported here involved the measurement of kinematic coincidences between projectile-like fragments (PLF's) and target-like fragments (TLF's) formed in the $E/A = 8.5$ MeV $^{74}\text{Ge} + ^{165}\text{Ho}$ reaction.

This projectile-target system possesses several advantages relative to our previous studies of the $^{56}\text{Fe} + ^{165}\text{Ho}$ system.¹⁰ (1) the atomic number of the projectile-like ($Z=32$) nuclei is sufficiently large to inhibit charged-particle decay of the excited fragments, thereby providing a good estimate of the primary Z values in terms of the measured PLF distributions; (2) both projectile and target nucleon numbers are well removed from closed shells, thus minimizing the influence of Q -value discontinuities in defining the potential-energy surface and in performing statistical decay calculations; and (3) the greater mass of ^{74}Ge relative to ^{56}Fe improves the resolution of the primary masses derived from the kinematic coincidence technique by reducing recoil effects. At the same time this projectile-target combination retains significant mass and N/Z asymmetry, which is valuable in testing the predictions of the nucleon exchange transport model.¹ Furthermore, the low fissility of the damped-reaction products reduces the number of events in which three heavy fragments appear in the exit channel.

The procedures followed in the experiment and subsequent data analysis are first discussed. We then present the experimental results for centroids and variances of all primary and post-evaporative Z , N , and A distributions determined in this work. Finally, a comparison with predictions of the nucleon exchange transport model for this system is performed. Monte Carlo simulations related to the data have been performed and are discussed in the companion paper.¹⁸

II. EXPERIMENTAL PROCEDURES

A. Detector system

The experiment was carried out at the Lawrence Berkeley Laboratory (LBL) SuperHILAC with beams of 100–200 enA ^{74}Ge ions incident upon a 205- $\mu\text{g}/\text{cm}^2$ ^{165}Ho target supported by a 100- $\mu\text{g}/\text{cm}^2$ carbon foil. The beam energy was $E/A = 8.5$ MeV/nucleon. During data acquisition, the target angle was oriented with the Ho side facing the heavy-recoil detector at an angle chosen to minimize energy-loss and multiple-scattering effects for the Ho-like recoil nuclei.

The mass, charge, energy, and angle of the post-evaporative projectile-like fragments (PLF's) were detected at a central angle of 26.5° with a time-of-flight ΔE - ΔE - E telescope. Time-of-flight information was obtained with a pair of microchannel-plate fast-timing detectors separated by 130 cm. Position, charge, and total energy were determined with an x - y position-sensitive ΔE - ΔE gas-ionization counter operated with CF_4 at 35 Torr, followed by a 900-mm² silicon surface-barrier E detector. The solid angle acceptance was 2.38 msr. Further details concerning the detector system can be found in Ref. 19.

Coincident target-like fragments (TLF's) were measured with an x - y position-sensitive multiwire proportional counter (MWPC) operated at 3.5 Torr of isobutane. This detector was collimated to provide an active area of 16.1 cm horizontally by 9.0 cm vertically and was located 27.5 cm from the target. The TLF detector was set at overlapping angles to span the entire angular range for

heavy recoils, which extended from 28° to 80° on the side of the beam opposite from the PLF telescope. The experimental full width at half maximum (FWHM) for TLF's in the heavy recoil detector was $\delta\theta \leq 1.1^\circ$; however, this function was non-Gaussian, as determined from examination of elastic recoils. This function summarizes effects due to (1) intrinsic angular resolution of the MWPC detector, (FWHM=0.4 $^\circ$); (2) scattering in the wire planes, gas and foils, as well as the angle of incidence of the TLF, (3) scattering of the TLF's in traversing the finite target thickness, and (4) the beam-spot size. The TLF resolution was determined experimentally by placing a $0.1^\circ \times 0.1^\circ$ window on ^{74}Ge elastic-scattering events in the PLF telescope (using the Z , A , and E FWHM values already quoted) and measuring the angular correlation function $C(\theta_{\text{TLF}})$ in the MWPC. The elastic TLF recoils constitute the worst case for determining MWPC and target resolution effects since these fragments possess the lowest kinetic energies and largest emission angles relative to the target normal. Thus, we believe the quoted errors are conservative ones. The experimental function for $C(\theta_{\text{TLF}})$ was subsequently used as a basis for determining the TLF resolution in subsequent Monte Carlo simulations of these data.¹⁸ A total of 1.3×10^6 coincident events were analyzed, 300 000 of these in the energy-loss range from 30 to 200 MeV.

B. Detector calibrations

In order to achieve the nuclide resolution required by the goals of this experiment, a detailed calibration procedure was followed.^{4,7,10,20} Subsequently, Monte Carlo simulations of the system were performed to evaluate potential sources of experimental and analytical bias (see the following paper, Ref. 18).

The initial step in the calibration procedure for the PLF telescope involved normalization of the silicon E detector with alpha-particle sources, elastically scattered beam particles, and a precision pulse generator. Corrections for pulse-height defect were included, as well as for the thickness of all foils in the fragment path and one-half the target thickness. Next, x - and y -position coordinates were determined from analysis of elastically scattered beam particles observed with a precision machined mask placed in front of the detector system during a calibration run. Position information was derived from the output of a time-to-digital converter that received start and stop signals from the silicon E detector and each gas-ionization element, ΔE_x and ΔE_y , respectively.

Nonlinearities in each segment of the ion chamber electronics were corrected on the basis of a pulse-generator calibration. The absolute energy calibrations of each gas-ionization chamber element, ΔE_x and ΔE_y , were obtained from energy-difference measurements of elastically scattered ^{74}Ge ions in the silicon detector, E_{Si} , recorded at a series of different gas pressures, P_i , in the ion chamber. Using this information, the following function was minimized with respect to calibration coefficients a and b :

$$\sum_i [E_{\text{Si}}(P=0) - E_{\text{Si}}(P_i) - a\Delta E_x(P_i) - b\Delta E_y(P_i)]^2. \quad (1)$$

The gas-ionization energy-loss signals, ΔE_x and ΔE_y , were found to be slightly position-dependent due to incomplete charge collection in some regions of the detector. Empirical correction matrices were constructed and corresponding corrections were applied to all events in order to incorporate this position-pulse-height dependence.¹⁰

Calibration of the dual channel-plate time-of-flight (TOF) system was performed with elastically scattered ^{74}Ge ions and a precision time calibrator. Corrections for variable flight path distances, $S(x,y)$, due to finite solid angle and tilted secondary emission foils, as well as a small position dependence of the electron travel time to the two channel-plate collecting electrodes, $\Delta t(x,y) \leq 60$ ps, were applied to the data. Fragment mass numbers, A , were then calculated using the expression

$$A = 2E \{ [\text{TOF} - \Delta t(x,y) - T_0] / S(x,y) \}^2. \quad (2)$$

Here TOF is the measured time of flight, T_0 is the time-of-flight offset due to cable length and electronics propagation delay differences, and E is the energy of the ion after passing through the carbon foil of the first channel plate. For fragments with $A = 74$, the experimental system yielded a resolution (FWHM) of $\delta A \leq 0.6$ u, $\delta Z \leq 0.6$ charge units, kinetic energy $\delta E \leq 6.5$ MeV, and $\delta\theta = 0.1^\circ$.

Position calibration for the heavy-recoil (TLF) detector was determined from the known wire spacings (2 mm) and the edges of the machined aperture frame mounted in front of the detector. In calibration runs with the coincidence requirements removed, both individual wires and frame edges were clearly identified. The absolute angles of the frame edges were determined via transit measurements to an accuracy of $\leq 0.1^\circ$. During production runs the absolute angle calibration could be readily monitored by the position of the elastic recoil peak.

In Fig. 1 (top) logarithmic cross-section contours are plotted which demonstrate the dependence of TLF recoil angle in the multiwire proportional counter as a function of PLF laboratory energy. One observes a strong peak at the kinematic angle expected for heavy recoils from the elastically scattered ^{74}Ge ions. With decreasing PLF energy, the most probable recoil angle shifts systematically to lower angles, consistent with expectations of a binary reaction mechanism. At very large energy losses one observes a nearly isotropic spreading of the TLF angular distribution, which we attribute to contributions from fusion-fission or sequential fission of the ^{165}Ho target. The dot-dashed line in Fig. 1 (top) is the kinematic locus of ^{165}Ho recoils from inelastic ^{74}Ge scattering with the corresponding laboratory energy.

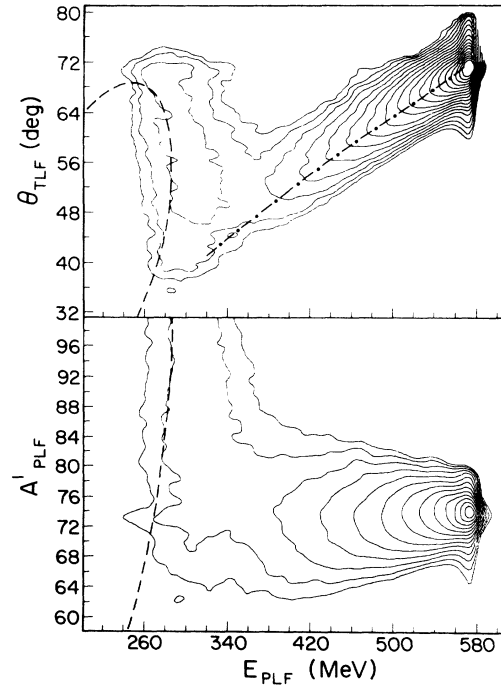


FIG. 1. Top: Logarithmic cross section contours for target-like fragment angle as a function of projectile-like fragment kinetic energy in the laboratory system. The average PLF angle is 26.5° . The dot-dashed line gives the kinematic locus expected for inelastically scattered ^{165}Ho recoil nuclei as a function of ^{74}Ge energy. The dashed line gives the estimated behavior of fusion-fission reactions, assuming a total kinetic energy release given by fission systematics (Ref. 23). Bottom: Smoothed cross section contours of PLF primary mass as a function of fragment kinetic energy in the laboratory system.

C. Primary mass and energy-loss determination

In order to determine primary mass and charge distributions, the data were analyzed with the assumption of a two-body primary reaction mechanism followed by isotropic light-particle evaporation from fully equilibrated fragments.^{10,21} The measured fragment angles and PLF time of flight for each event completely determine the kinematics of the primary reaction, when averaged over a large number of similar events, thus determining the masses of the primary fragments, A' , prior to light-particle evaporation. (Hereafter, primed quantities refer to primary yields and unprimed quantities to the post-evaporative yields.) When neutron multiplicities determined with this technique are compared with directly measured values²² for the $^{56}\text{Fe} + ^{165}\text{Ho}$ system they are found to be in good agreement.¹⁰

For each event we have calculated the primary mass by the equation:

$$A'_{\text{PLF}} = A_p v_p / v_{\text{PLF}} [\cos\theta_{\text{PLF}} + (\sin\theta_{\text{PLF}})(\cot\theta_{\text{TLF}})(\cos\phi_{\text{PLF}}) / \cos\phi_{\text{TLF}}], \quad (3)$$

where A_p is the projectile mass and v_p and v_{PLF} are the projectile and PLF velocities, respectively. Corresponding scattering angles for the PLF and TLF in the laboratory system are given by θ and ϕ in polar coordinates. In

Fig. 1 (bottom) logarithmic cross-section contours are shown for the primary PLF masses deduced in this way. The intrinsic nuclide resolution has been smoothed in this plot for visual representation of the average trends of the

data and to derive average parameters of the distributions using a two-dimensional Gaussian fitting function.^{4,20}

The most probable PLF mass values remain essentially the same as that of the projectile, with a slight decrease in mass observed with increasing energy loss. For very large energy losses, a spreading of the mass distribution toward symmetry occurs due to a growth in the fission component. The dashed line in this figure gives the predicted kinematic behavior for fusion-fission fragments, assuming fission fragment kinetic energy release systematics.²³

The kinetic energy for each primary PLF was approximated by

$$E'_{\text{PLF}} = E_{\text{PLF}} A'_{\text{PLF}} / A_{\text{PLF}}, \quad (4)$$

where A' and A refer to the reconstructed (primary) and measured (post-evaporative) masses, respectively. The total kinetic energy loss, E_{loss} , was then calculated using the reconstructed PLF primary mass and kinetic energy and the measured PLF angle.

Fragment primary charges, Z'_{PLF} , and excitation energy, E^*_{PLF} , were derived via an iterative event-by-event analysis based on statistical-model predictions of the PACE-II code.²⁴ Details of this procedure can be found in the following paper and in Ref. 10. The primary and measured charge distributions are found to be nearly equivalent for this system. These calculations indicate

that $\langle \Delta Z_{\text{PLF}} \rangle = \langle Z'_{\text{PLF}} \rangle - \langle Z_{\text{PLF}} \rangle \approx 0.2$ charge units at an energy loss of 150 MeV.

Monte Carlo simulations have been performed on these data, taking into account all experimental resolutions and the charge and mass distributions of the fragments (see the following paper¹⁸). These simulations indicate a mass resolution $\delta A'$ (FWHM) for the primary fragments that is approximately $\delta A' \approx 1.3$ u for elastic PLF's and varies thereafter according to a function of the form $\delta A' = 1.6 \times 10^{-3} E_L^{3/2} + 1.3$. In addition, these studies demonstrate that the centroids of the primary kinetic energy distributions of the fragment and E_{loss} are well reproduced by our event-by-event method. The same conclusion holds for the centroids and variances of the mass and charge distributions.

III. FRAGMENT NUCLIDE DISTRIBUTIONS

A. General features

In order to gain a qualitative overview of the nucleon exchange and N/Z equilibration processes, it is instructive to examine the general evolution of the measured fragment nuclide distributions as a function of atomic number, mass number, and energy loss.

In Fig. 2 the measured (post-evaporative) isotopic distributions for $Z = 27-35$ fragments are shown for the

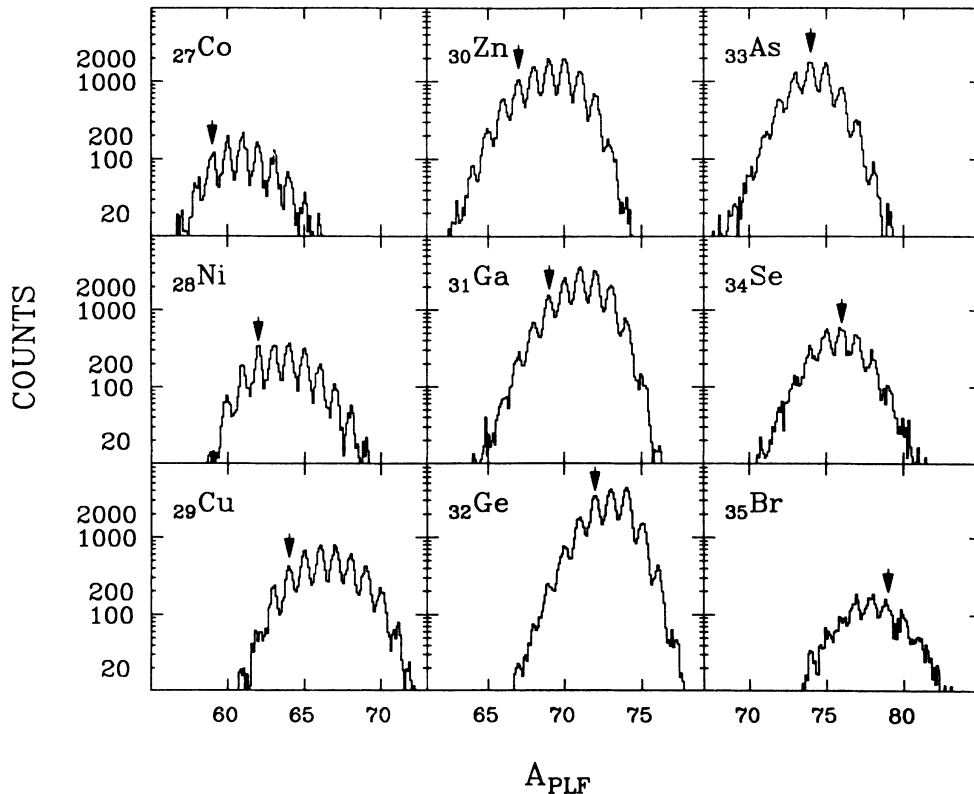


FIG. 2. Isotopic distributions for several PLF atomic numbers, as indicated on the figure. Centroid of beta stability is indicated by an arrow for each case. Data span the energy-loss range 30–200 MeV.

energy-loss range $E_{\text{loss}} = 30\text{--}200$ MeV (i.e., quasielastic and fission-like events are excluded). The bulk of the cross section is concentrated in the $Z = 30\text{--}33$ yields. It is noted that the centroid of each distribution relative to the N/Z ratio corresponding to the line of beta stability (indicated by arrow) depends sensitively on whether nucleons are gained or lost during the interaction and subsequent decay. For atomic numbers lower than the projectile ($Z < 32$), the isotopic distributions become increasingly dominated by neutron-excess isotopes. Higher atomic numbers exhibit the opposite behavior, i.e., the yields favor neutron deficient isotopes. Since proton decay is relatively unimportant for these data, the results suggest that the excitation energies of the PLF's with $Z > 32$ are significantly larger than those for $Z < 32$ (thereby enhancing neutron decay). This observation concerning the N/Z ratios and the approximately Gaussian shape of the isotopic distributions have important implications for the synthesis of exotic and neutron-rich isotopes by means of low-energy damped collisions such as these. For PLF's, only elements with $Z < Z_{\text{proj}}$ will populate neutron-rich nuclei with meaningful probabilities. For TLF fragments with $Z > Z_{\text{targ}}$ neutron-deficient products will be favored, thus populating those nuclei that can be readily reached via more conventional reactions. Further, as discussed in the following paper,¹⁸ the excitation-energy distributions behave in such a way as to inhibit the observation of exotic species formed by multinucleon pickup reactions. It is only the rather broad variances of all these distributions that permit observation of rare nuclei in damped collisions.²⁵

Figure 3 presents the post-evaporative mass distributions as a function of energy loss for 20-MeV energy-loss bins that extend from the quasielastic region to nearly fully damped events. The systematic broadening of the mass distributions as a function of energy loss, characteristic of the damped collision process,^{8,9} is clearly illustrated in these data. As the energy loss increases, the mass centroid of each distribution shifts to lower A values, reflecting the combined effects of nucleon exchange from the projectile to target and the decay of the excited primary fragments. The narrow, Gaussian-like behavior of the yield curves at low E_{loss} values becomes increasingly skewed toward heavier masses at the largest energies due to the growth in importance of long time-scale mechanisms such as fission.

The evolution of the full nuclide distributions with energy loss is shown in Fig. 4 for representative energy-loss bins (± 5 MeV) that span the full range of events where damped collisions dominate the cross section. Here, cross-section contours in the N vs Z plane are presented for the post-evaporative fragments, where $N = A - Z$. The solid dots represent the projectile N and Z values. At $E_{\text{loss}} = 30$ MeV, where little energy is available for decay of the primary fragments, it is apparent that the net transfer of one neutron and/or proton from projectile to target is much stronger than transfers in the opposite direction. With increasing energy loss the contours broaden due to the combined effects of nucleon exchange and statistical decay of the primary fragments. Most noticeable in the evolution of these distributions is the

strong preference for proton transfer from projectile to target with increasing energy, and the gradual alignment with the N/Z ratio corresponding to the line of maximum beta stability. This behavior is similar to that reported previously for several lighter systems.^{4,6,7} A two-dimensional Gaussian fitting procedure has been applied to these distributions (described more fully in Refs. 4, 7, and 20). From a least-squares fit centroids ($\langle Z \rangle$, $\langle N \rangle$, and $\langle A \rangle$), variances (σ_Z^2 , σ_N^2 , and σ_A^2), and neutron-proton correlation coefficients (ρ_{NZ}) were generated. These fit values are summarized in Table I for the measured data and Table II for the reconstructed primary data. Additionally, conditional variances $\sigma_Z^2(N)$, $\sigma_N^2(Z)$, and $\sigma_Z^2(A)$ were generated from the data. Tables III and IV present these results in terms of the parameters of a two-dimensional Gaussian fitting function.²⁰

B. Centroids and variances

In Fig. 5 the centroids for the Z , N , and A distributions are plotted, along with the $\langle N \rangle / \langle Z \rangle$ ratio, as a function of energy loss. The circles represent the primary A' and N' distributions reconstructed from the coincidence data; squares show the measured (post-

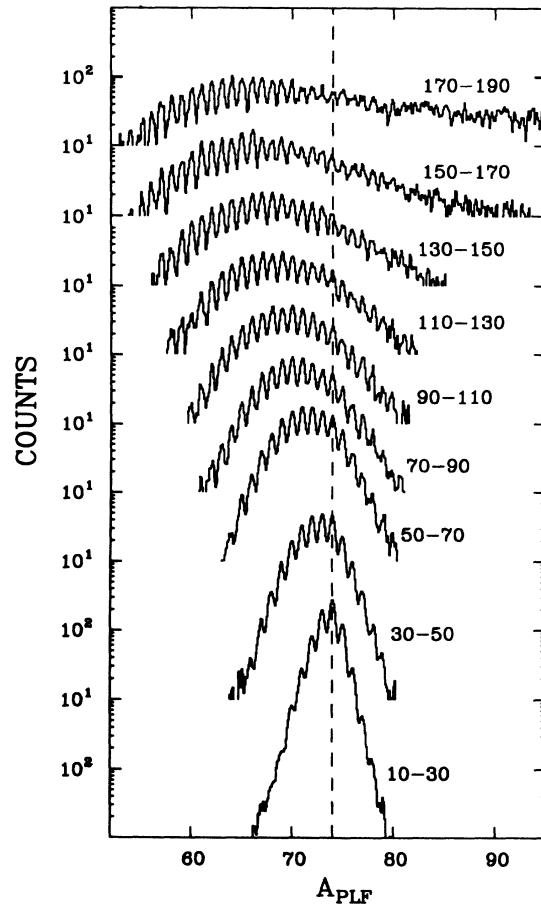


FIG. 3. Mass distributions as a function of energy loss, as indicated on figure. Dashed line is $A = 74$.

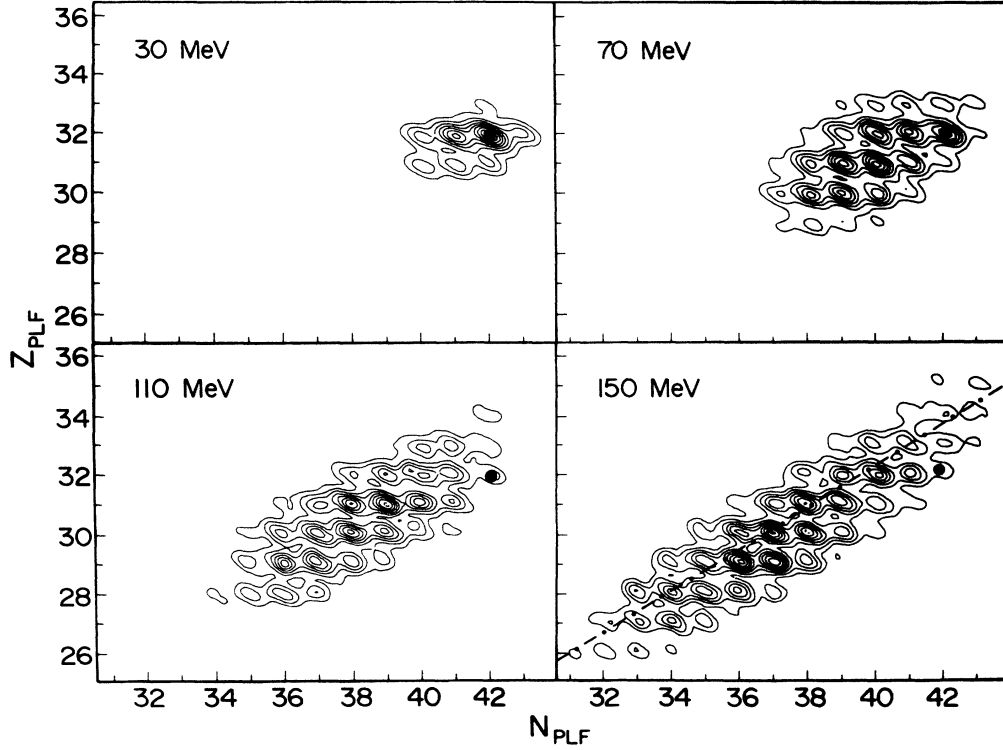


FIG. 4. Cross section contours in the N vs Z plane for the ${}^{74}_{32}\text{Ge} + {}^{165}_{67}\text{Ho}$ reaction at several representative energy losses. Each bin width is ± 5 MeV about the centroid. The dot-dashed line shows the line of maximum beta stability. Solid dot is ${}^{74}\text{Ge}$.

TABLE I. Parameters of measured post-evaporative yield distribution for projectile-like fragments for the $E/A = 8.5$ MeV ${}^{74}\text{Ge} + {}^{165}\text{Ho}$ reaction.

E_{loss} (MeV)	$\langle Z \rangle$	$\langle N \rangle$	σ_Z^2	σ_N^2	ρ_{NZ}
4	31.83±0.06	41.83±0.09	0.193±0.022	0.549±0.081	-0.224±0.086
8	31.84±0.06	41.74±0.08	0.203±0.018	0.741±0.082	-0.081±0.077
12	31.83±0.05	41.67±0.08	0.233±0.015	0.87±0.066	-0.001±0.056
16	31.81±0.05	41.57±0.08	0.278±0.018	1.01±0.068	0.088±0.048
20	31.76±0.06	41.45±0.10	0.377±0.022	1.16±0.075	0.102±0.044
24	31.69±0.06	41.22±0.10	0.520±0.067	1.54±0.16	0.136±0.075
28	31.55±0.06	41.10±0.09	0.832±0.071	1.71±0.16	0.175±0.058
32	31.48±0.06	40.92±0.09	0.956±0.085	1.70±0.14	0.191±0.057
36	31.41±0.07	40.77±0.09	1.06±0.096	1.97±0.16	0.241±0.057
40	31.42±0.07	40.63±0.09	1.27±0.10	2.07±0.14	0.280±0.050
44	31.33±0.07	40.45±0.09	1.38±0.10	2.21±0.15	0.305±0.047
48	31.26±0.07	40.32±0.09	1.47±0.10	2.55±0.16	0.360±0.043
52	31.23±0.07	40.16±0.09	1.55±0.10	2.58±0.17	0.408±0.041
56	31.19±0.07	39.99±0.09	1.64±0.11	2.82±0.18	0.425±0.041
60	31.12±0.07	39.83±0.09	1.87±0.13	3.08±0.20	0.456±0.040
64	31.04±0.07	39.67±0.09	1.89±0.13	3.18±0.21	0.485±0.040
70	30.98±0.07	39.44±0.09	2.13±0.12	3.53±0.19	0.517±0.031
80	30.85±0.07	39.08±0.09	2.45±0.13	4.04±0.22	0.582±0.027
90	30.74±0.07	38.75±0.09	2.82±0.15	4.85±0.25	0.640±0.023
100	30.62±0.07	38.39±0.09	3.23±0.16	5.72±0.27	0.710±0.018
110	30.42±0.08	38.01±0.11	3.84±0.30	6.86±0.53	0.732±0.026
120	30.27±0.08	37.66±0.11	3.94±0.28	7.46±0.54	0.761±0.023
130	30.13±0.09	37.29±0.12	5.01±0.38	9.17±0.69	0.821±0.019
140	30.09±0.09	37.21±0.12	5.92±0.41	10.5±0.71	0.848±0.015
150	29.91±0.10	36.86±0.13	7.00±0.48	12.3±0.86	0.867±0.013
160	29.88±0.10	36.73±0.14	8.39±0.56	15.5±1.0	0.894±0.010
170	30.01±0.11	36.81±0.15	10.2±0.71	18.7±1.3	0.913±0.009
180	30.64±0.12	37.53±0.17	15.8±1.0	29.0±1.8	0.941±0.005

evaporative) results. Primary Z' values were obtained from fitting the difference between the primary and secondary masses using the PACE-II statistical evaporation code.²⁴ The experimental primary distributions in Fig. 5 demonstrate that the net transfer of protons from the PLF to the TLF is favored in this reaction; in contrast, the net neutron transfer is small. The result is a weak drift toward mass *asymmetry*. This behavior is in general agreement with the trends observed in several other inclusive measurements of PLF nuclide distributions from mass-asymmetric projectile target systems.^{4–9,26} In fact, the magnitude of both the proton and neutron drifts is quite similar to the behavior of the $^{64}\text{Ni}+^{238}\text{U}$ system⁷ at this energy; ^{64}Ni and ^{74}Ge have nearly identical N/Z values. The average neutron/proton ratio for the primary fragments gradually increases with increasing energy loss and evolves toward, but does not reach, the N/Z of the composite system (^{239}Es : $N/Z = 1.41$). Data beyond $E_{\text{loss}} = 180$ MeV are not given for the centroids due to the increasing contributions of fission-like events, which cannot be fully included due to the upper Z and A values accepted by our detection system ($Z_{\text{max}} \approx 38$; $A_{\text{max}} \approx 85$).

The variances of the Z , N , and A distributions are presented in Fig. 6 for both the primary and measured values. The variances, which are related to the total number of nucleon exchanges in statistical transport models, are found to increase monotonically for all distributions as a function of increasing energy loss and are

distinctly broader for the primary distributions relative to the experimentally observed values. This narrowing of the distributions during nucleon decay is imposed by the potential energy surface of the PLF's, which focuses the decay products toward the valley of beta stability. For highly damped events, the variances increase rapidly, consistent with expectations for a system that has nearly reached full thermal equilibrium. When compared with data for similar heavy targets at bombarding energies near $E/A = 8.5$ MeV, the variances for the $^{74}\text{Ge}+^{165}\text{Ho}$ reaction are systematically larger than those for lighter projectiles and smaller than those for heavier projectiles at the same energy-loss values.^{4–7,27}

Figure 7 (top) presents the ratio of the neutron-to-proton variances as a function of energy loss. For reactions which involve more than about 30 MeV of energy damping, this ratio is nearly constant for both primary and post-evaporative fragment yields. In the quasielastic region a marked increase in the σ_N^2/σ_Z^2 ratio is observed. This behavior can be attributed to the negative Q values for transfer of protons from projectile to target in this reaction, while neutron transfer is not similarly inhibited in either direction. Hence, the larger number of available channels for neutron transfer relative to those for proton transfer leads to larger neutron variances in this region of limited available excitation energy.

Figure 7 (bottom) shows the neutron-proton correlation coefficients, ρ_{NZ} , derived from the two-dimensional Gaussian fits to the data as a function of energy loss.

TABLE II. Parameters of primary yield distribution for projectile-like fragments derived from kinematic coincidences for the $E/A = 8.5$ MeV $^{74}\text{Ge}+^{165}\text{Ho}$ reaction.

E_{loss} (MeV)	$\langle Z' \rangle$	$\langle N' \rangle$	$\sigma_{Z'}^2$	$\sigma_{N'}^2$	$\rho_{NZ'}$
20	31.75±0.06	41.61±0.09	0.366±0.038	1.89±0.18	0.115±0.064
24	31.70±0.06	41.60±0.08	0.462±0.036	1.96±0.14	0.128±0.044
28	31.53±0.06	41.60±0.08	0.841±0.048	2.39±0.15	0.204±0.038
32	31.47±0.06	41.56±0.08	0.934±0.051	2.64±0.15	0.236±0.034
36	31.39±0.06	41.55±0.08	1.04±0.062	2.83±0.15	0.289±0.036
40	31.39±0.06	41.63±0.08	1.29±0.078	3.27±0.17	0.336±0.035
44	31.30±0.06	41.59±0.08	1.35±0.067	3.32±0.14	0.353±0.029
48	31.25±0.06	41.58±0.08	1.45±0.069	3.67±0.17	0.403±0.028
52	31.20±0.06	41.56±0.09	1.52±0.071	4.19±0.20	0.428±0.027
56	31.16±0.06	41.53±0.09	1.64±0.079	4.51±0.21	0.445±0.027
60	31.08±0.06	41.47±0.09	1.82±0.090	4.56±0.22	0.487±0.027
64	31.01±0.06	41.39±0.09	1.88±0.097	4.81±0.24	0.475±0.028
70	30.94±0.06	41.38±0.08	2.04±0.081	5.60±0.22	0.518±0.021
80	30.80±0.06	41.35±0.08	2.36±0.086	6.35±0.22	0.561±0.018
90	30.71±0.06	41.35±0.09	2.73±0.097	7.61±0.26	0.605±0.016
100	30.59±0.06	41.36±0.09	3.20±0.10	8.92±0.30	0.651±0.014
110	30.53±0.07	41.24±0.10	4.17±0.19	10.1±0.47	0.660±0.019
120	30.37±0.07	41.08±0.10	4.55±0.21	11.5±0.55	0.704±0.018
130	30.27±0.07	41.00±0.11	5.64±0.28	14.2±0.72	0.733±0.017
140	30.17±0.08	41.06±0.11	6.68±0.34	16.0±0.81	0.746±0.017
150	30.10±0.09	41.07±0.13	8.43±0.45	19.8±1.1	0.772±0.016
160	30.10±0.09	41.17±0.14	8.29±0.47	21.0±1.2	0.785±0.016
170	30.37±0.10	41.69±0.15	11.8±0.65	30.2±1.6	0.803±0.014
180	30.79±0.14	42.27±0.20	14.5±1.1	37.3±2.9	0.829±0.016

Values of $\rho_{NZ} > 0$ correspond to correlated neutron-proton exchange and are indicative of a statistical nucleon-exchange mechanism confined by Q -value constraints to the valley of beta stability. Values of $\rho_{NZ} = 0$ represent uncorrelated exchange. Values of $\rho_{NZ} < 0$ signify anticorrelated nucleon exchange, which may be associated with fast charge exchange mechanisms in the early stages of the projectile-target interaction.^{28,29} The data shown in the lower part of Fig. 7 increase monotonically from $\rho_{NZ} \leq 0$ at low-energy losses to values near $\rho_{NZ} \approx 1$ for fully damped events. The slightly negative values of ρ_{NZ} at very-low-energy losses must be interpreted with caution due to the small number of species which comprise the nuclide distributions, which subsequently complicates the extraction of ρ_{NZ} .⁷

Finally, in Fig. 8 the energy-loss dependence of the conditional variances is presented for the proton distribution at constant neutron number, $\sigma_Z^2(N)$; the neutron distribution at constant atomic number, $\sigma_N^2(Z)$, and the isobaric proton distribution, $\sigma_Z^2(A)$. These values have also

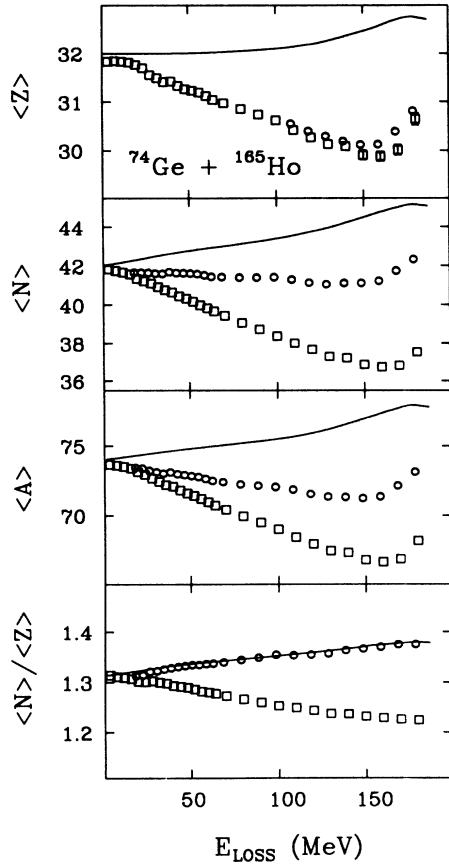


FIG. 5. Centroids of the Z , N , and A distributions and the $\langle N \rangle / \langle Z \rangle$ ratio for PLF's as a function of energy loss. Squares indicate measured post-evaporative values, circles give the primary values reconstructed from the kinematic coincident technique, and the solid line is the prediction of the nucleon exchange transport model (Ref. 1).

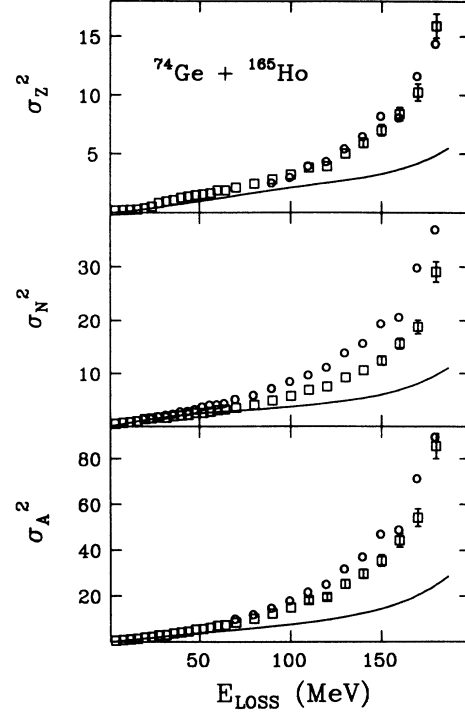


FIG. 6. Variances of the Z , N , and A distribution for PLF's as a function of energy loss. Symbols are the same as in Fig. 5.

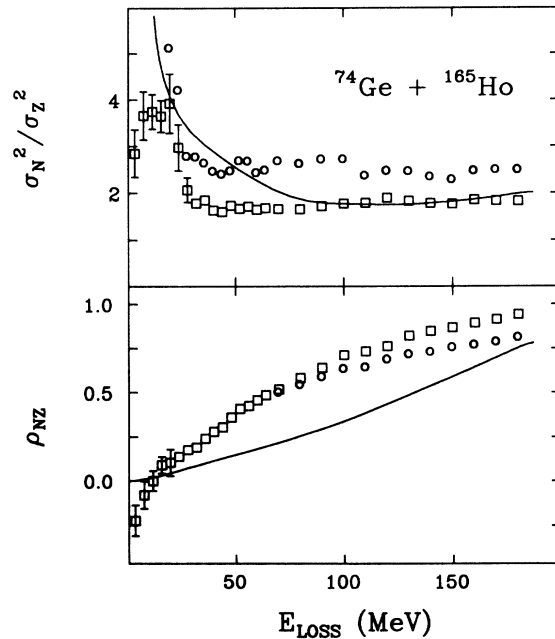


FIG. 7. Top: Ratio of the neutron variance to proton variance as a function of energy loss; Bottom: neutron-proton correlation coefficient as a function of energy loss. Symbols are the same as Fig. 5. Statistical errors are approximately the same size as the data points.

been derived from two-dimensional Gaussian fits to the Z , N , and A distributions. The post-evaporative conditional variances are larger but similar in both magnitude and E_{loss} dependence to those for lighter systems; i.e., the values of $\sigma_Z^2(N)$ and $\sigma_Z^2(A)$ increase rapidly up to ≈ 30 MeV of E_{loss} and remain nearly constant thereafter; values of $\sigma_N^2(Z)$ increase more gradually.

IV. COMPARISON WITH TRANSPORT MODEL CALCULATIONS

Several transport models have been proposed to account for the experimental observables in damped collisions, each involving somewhat different mechanisms for energy dissipation.¹⁻³ Here we compare the data for the $^{74}\text{Ge} + ^{165}\text{Ho}$ system with the nucleon exchange transport model of Randrup.¹ In this model all dissipative and transport phenomena are attributed to the exchange of independent nucleons between the reaction partners. Mutual excitations due to mean-field and collective effects are neglected. The salient transport coefficients are calculated in the classical limit from the instantaneous

condition of the dinuclear complex, assuming the constituents are always in intrinsic thermodynamic equilibrium. The reaction variables include the charge Z and mass A of the fragments. The average values of the macroscopic coordinates and velocities follow the equations of motion determined by the Lagrange-Rayleigh equations. The driving forces affecting the evolution of the collective variables can be separated into static and dynamic components.^{1,9}

In this model, the fluctuations in N and Z about the average values are predicted by a Fokker-Planck equation,

$$\frac{\partial}{\partial t} P(N, Z, t) = \left[-\frac{\partial}{\partial N} v_N - \frac{\partial}{\partial Z} v_Z + \frac{\partial^2}{\partial N^2} D_{NN} + \frac{\partial^2}{\partial Z^2} D_{ZZ} \right] P(N, Z, t), \quad (5)$$

describing the time dependence of the joint probability distribution $P(N, Z, t)$ for finding N neutrons and Z protons at time t in one of the reaction partners. Drift and

TABLE III. Two-dimensional Gaussian-fit parameters of the measured post-evaporative yield distribution for the $^{74}\text{Ge} + ^{165}\text{Ho}$ system. The parameters a' and b' represent the minor and major axes of the ellipses representing the two-dimensional N vs Z distributions; k gives the slope of the major ellipses axis with respect to the N axis. These parameters permit calculation of all possible variances and correlation coefficients according to relationships given in Ref. 20.

E_{loss} (MeV)	a' (obs)	b' (obs)	k (obs)
4	5.59±0.61	1.774±0.263	-0.197±0.077
8	4.97±0.43	1.346±0.149	-0.058±0.056
12	4.30±0.27	1.149±0.0871	-0.001±0.039
16	3.63±0.23	0.983±0.0663	0.064±0.035
20	2.69±0.15	0.856±0.0553	0.086±0.038
24	1.97±0.25	0.642±0.0704	0.117±0.065
28	1.27±0.11	0.567±0.0546	0.225±0.075
32	1.13±0.10	0.563±0.0485	0.297±0.088
36	1.05±0.09	0.477±0.0395	0.341±0.080
40	0.938±0.078	0.438±0.0309	0.450±0.082
44	0.891±0.070	0.403±0.0281	0.490±0.078
48	0.882±0.068	0.344±0.0223	0.491±0.061
52	0.906±0.068	0.329±0.0215	0.552±0.059
56	0.872±0.067	0.301±0.0197	0.547±0.056
60	0.814±0.061	0.267±0.0180	0.592±0.054
64	0.842±0.067	0.256±0.0167	0.597±0.057
70	0.800±0.051	0.226±0.0126	0.621±0.040
80	0.800±0.050	0.190±0.0104	0.655±0.036
90	0.793±0.047	0.155±0.0081	0.659±0.030
100	0.848±0.047	0.128±0.0062	0.671±0.023
110	0.769±0.063	0.106±0.0083	0.676±0.035
120	0.822±0.068	0.0981±0.0071	0.661±0.029
130	0.868±0.076	0.0767±0.0058	0.694±0.027
140	0.872±0.069	0.0653±0.0044	0.714±0.023
150	0.848±0.064	0.0549±0.0038	0.721±0.020
160	0.869±0.064	0.0438±0.0029	0.709±0.017
170	0.874±0.067	0.0359±0.0025	0.718±0.015
180	0.826±0.058	0.0228±0.0015	0.726±0.012

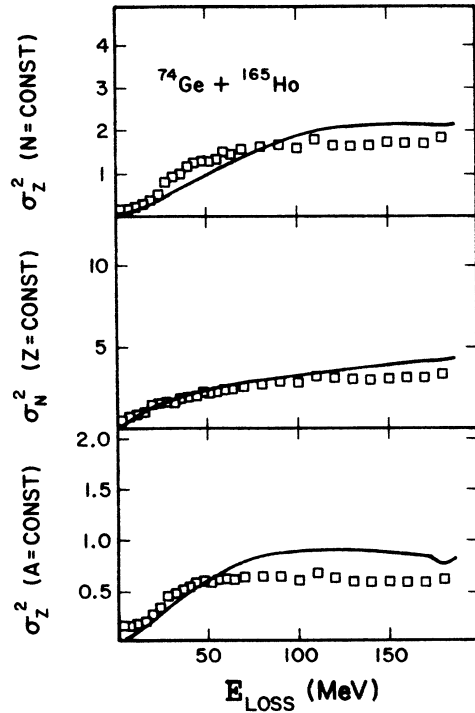


FIG. 8. Conditional variances as a function of energy loss. The top figure shows charge variance at fixed neutron number; the central figure is neutron variance at fixed charge, and the bottom figure gives charge variance at fixed mass number. Symbols are the same as in Fig. 5.

diffusion coefficients, ν and D , respectively, have been calculated microscopically by Randrup.¹ The preceding dynamical transport calculation gives the first and second moments of the proton (Z) and neutron (N) number distributions, as well as the temperatures of the primary reaction fragments.

The results of these calculations are shown as solid lines in Figs. 5–10. Comparison of the centroids of the experimental primary distributions in Fig. 5 with calculated centroids based on the nucleon exchange transport model reveals a significant deviation. The model calculations predict very little net proton transfer over nearly the full energy-loss region, accompanied by the net pick-up of neutrons by the PLF. This produces a mass drift toward mass *symmetry*. In contrast, the data reveal that proton transfer from projectile to target dominates the net exchange of nucleons, while little net neutron exchange occurs. This produces a mass drift toward *asymmetry*. The experimental and calculated centroid ratios, $\langle N \rangle / \langle Z \rangle$, in Fig. 5 agree rather well, despite the discrepancies between the measured and predicted centroids.

This discrepancy between experiment and theory is illustrated more transparently in Fig. 9 where the evolution of the centroids of the nuclide distributions in the N versus Z plane is plotted for successive energy-loss bins up to 180 MeV of energy loss. The squares represent the post-evaporative measured data; open circles are the kinematically reconstructed primary data. The dash-dotted line shows the valley of beta stability in this region; the dotted line is the N/Z ratio of the composite

TABLE IV. Two-dimensional Gaussian-fit parameters of the primary nuclide distributions derived from kinematic coincidences yield distribution for the $^{74}\text{Ge} + ^{165}\text{Ho}$ system, as described in Table III.

E_{loss} (MeV)	a' (primary)	b' (primary)	k (primary)
20	2.77 ± 0.28	0.525 ± 0.0500	0.062 ± 0.035
24	2.21 ± 0.17	0.505 ± 0.0361	0.080 ± 0.028
28	1.26 ± 0.072	0.408 ± 0.0272	0.180 ± 0.033
32	1.16 ± 0.065	0.367 ± 0.0218	0.207 ± 0.030
36	1.08 ± 0.068	0.337 ± 0.0190	0.260 ± 0.032
40	0.929 ± 0.060	0.286 ± 0.0153	0.315 ± 0.034
44	0.910 ± 0.048	0.279 ± 0.0124	0.336 ± 0.028
48	0.899 ± 0.045	0.249 ± 0.0116	0.363 ± 0.026
52	0.876 ± 0.042	0.218 ± 0.0106	0.354 ± 0.024
56	0.832 ± 0.041	0.201 ± 0.0095	0.367 ± 0.024
60	0.810 ± 0.040	0.194 ± 0.0097	0.423 ± 0.026
64	0.767 ± 0.040	0.185 ± 0.0092	0.408 ± 0.027
70	0.756 ± 0.031	0.158 ± 0.0063	0.409 ± 0.019
80	0.710 ± 0.027	0.136 ± 0.0049	0.440 ± 0.016
90	0.672 ± 0.027	0.112 ± 0.0040	0.451 ± 0.014
100	0.643 ± 0.023	0.0946 ± 0.0032	0.473 ± 0.013
110	0.518 ± 0.027	0.0806 ± 0.0038	0.522 ± 0.019
120	0.536 ± 0.028	0.0702 ± 0.0034	0.527 ± 0.017
130	0.478 ± 0.025	0.0562 ± 0.0029	0.541 ± 0.018
140	0.428 ± 0.024	0.0489 ± 0.0025	0.562 ± 0.018
150	0.379 ± 0.021	0.0390 ± 0.0022	0.581 ± 0.017
160	0.400 ± 0.024	0.0372 ± 0.0022	0.559 ± 0.017
170	0.306 ± 0.018	0.0258 ± 0.0014	0.563 ± 0.016
180	0.284 ± 0.018	0.0207 ± 0.0016	0.572 ± 0.019

system (^{239}Es), and the solid line is the result of the nucleon exchange transport model¹ for the corresponding energy-loss range. Figure 9 demonstrates that for this particular system, the direction of net neutron and proton drift for the experimental data is nearly opposite that for the model calculations. This discrepancy between experiment and theory has been previously observed on a less pronounced scale for lighter projectiles^{6,7,10} such as $^{40,48}\text{Ca}$, ^{56}Fe , and $^{58,64}\text{Ni}$. However, in these cases the primary A' values were derived from evaporative corrections to the secondary data. The present results examine the model predictions with experimentally determined primary A' values that do not rely on any assumptions other than that of a binary reaction mechanism and isotropic emission of emitted particles during deexcitation. Nonetheless, the results determined here confirm previous conclusions that net nucleon exchange in damped collisions is not adequately accounted for by current transport model calculations. It should be recalled, however, that the net nucleon drift represents a small difference between two large opposite currents of nucleons.

In Fig. 10 the nuclide evolution in the N versus Z plane is compared for the $^{58}\text{Ni} + ^{238}\text{U}$, $^{64}\text{Ni} + ^{238}\text{U}$, $^{56}\text{Fe} + ^{165}\text{Ho}$,

and $^{74}\text{Ge} + ^{165}\text{Ho}$ systems. For the two reactions with ^{165}Ho , primary data are derived from the kinematic coincidence technique; for the two Ni-induced reactions, primary data were obtained from evaporation corrections to the primary data, assuming excitation energy division as given by the nucleon exchange transport model. For reference we have also included the vector indicating the direction and the magnitude of the gradient of the potential energy surface for each of these systems at the injection point. The length of each gradient vector is indicative of the strength of the potential gradient. Calculation of the potential energy surfaces were performed according to the relation

$$V = V_{\text{PLF}}^{\text{LD}} + V_{\text{TLF}}^{\text{LD}} + V_N + V_L - V_C, \quad (6)$$

where V_i^{LD} is the liquid-drop (LD) binding energy with shell corrections but suppression of pairing effects of the PLF and TLF, as calculated from Myers.³⁰ The nuclear potential V_N was also based on the liquid-drop model with the modified proximity potential of Swiatecki.³¹ The effective centrifugal potential, V_L , and the Coulomb potential, V_C , were those assumed in the transport model of Ref. 1.

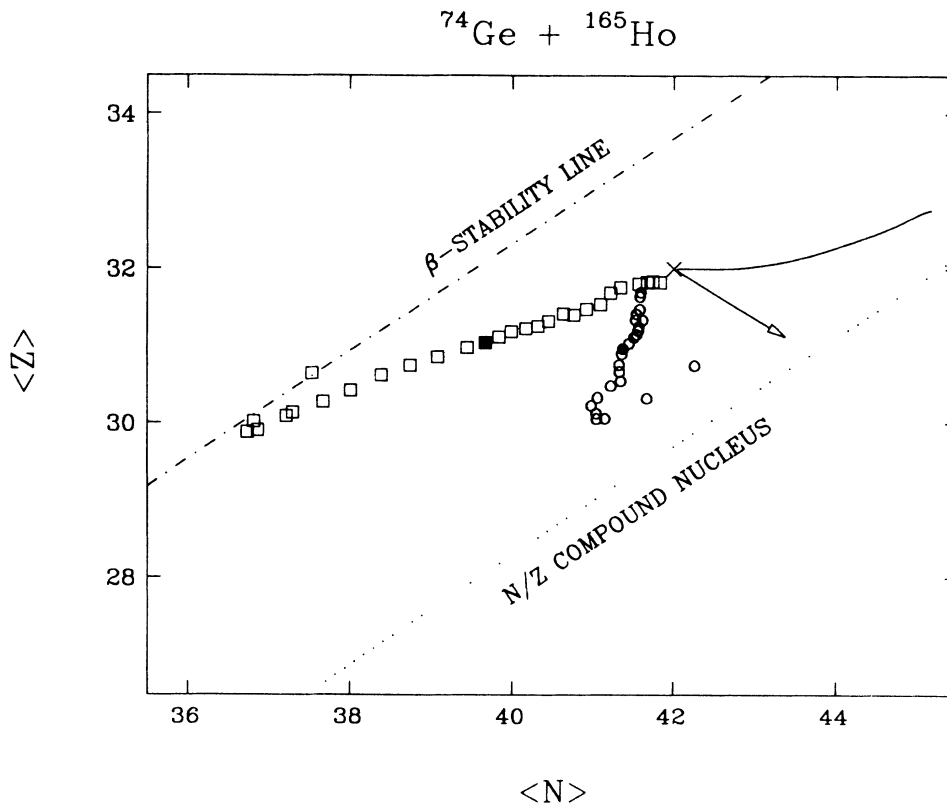


FIG. 9. Evolution of the centroids of the nuclide distributions in the N - Z plane as a function of energy loss. The target-projectile injection point at zero-energy loss is indicated by the cross (x). Energy damping proceeds sequentially in 4-MeV steps up to 64 MeV (solid points) and in 10-MeV steps from 70 to 180 MeV of energy loss thereafter. Measured distributions are indicated by squares, primary distributions by circles and theoretical predictions (Ref. 1) by the solid line.

Here we assume the sticking condition for calculation of V_L . The total potential was normalized to zero at the injection point. The gradients shown in Fig. 10 were calculated for angular momenta just below the grazing value for a projectile-target distance

$$r = (R_{1/2})_T + (R_{1/2})_P + 0.2 \text{ fm} . \quad (7)$$

These gradients depend only slightly on the interaction radius; for example, for the half-density radius $r = R_{1/2}$ or $r = R_{SA}$, the magnitude of the gradient vector changes only about 10%. Comparison of the four systems in Fig. 10 reveals that for the $^{58}\text{Ni} + ^{238}\text{U}$ system⁷ (where the gradient is strongest), the evolution of the neutron and proton centroids as a function of energy loss follows the gradient in the potential rather closely. For the $^{74}\text{Ge} + ^{165}\text{Ho}$ system, proton exchange is considerably stronger than predicted by the gradients.

In all cases the model indicates preferential neutron transfer from target to projectile and relatively little proton exchange. The difference between the direction of the gradient and that of the model appears to be largely due to the dynamical driving forces in the nucleon exchange transport model. Thus, these results suggest the need to reexamine this aspect of the theory. Recent Monte Carlo transport calculations of Tassan-got *et al.*,³² which include temperature and angular momentum equilibration

terms, provide an improved description of the experimental mass drift toward asymmetry. However, detailed agreement with the data is still not found.

Comparison of the second moments of the distributions (Fig. 6) reveals that the model calculations underpredict the variances by a significant amount, especially for the neutron variances. This behavior is in contrast with data with lighter projectiles, for which the agreement is relatively good. In Fig. 11 the ratios of the experimental to calculated variances of the primary charge distributions at 100 MeV of energy loss are plotted versus a target-projectile mass asymmetry parameter $(A_T - A_P)/(A_P + A_T)$ for several projectiles incident on heavy targets ($A_T \geq 120$). The systems included here all were measured at a bombarding energy of $E/A \approx 8.5$ MeV and were selected from studies where the primary fragment properties could be estimated without major uncertainties due to evaporative corrections, or from heavy systems in which the primary and post-evaporative charge variances should be nearly identical.^{4,5,33-35} This analysis suggests that for relatively asymmetric systems, the calculated and measured variances agree rather well. For more symmetric reaction partners, the experimental widths grow more rapidly than the calculated values, thus leading to a ratio greater than unity. Similar discrepancies—particularly at high-energy loss values—are observed in Figs. 7 and 8 for the ratio of the vari-

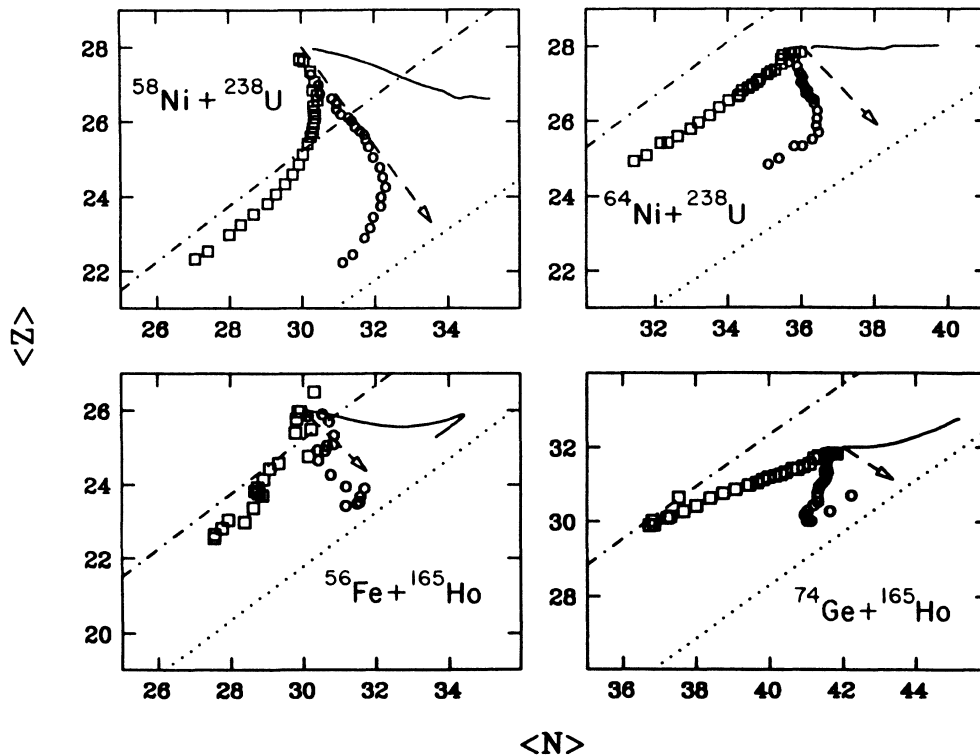


FIG. 10. Evolution of net nucleon exchange as a function of energy loss for four systems, as defined on figure. Symbols are the same as in Fig. 9. Dot-dashed lines show the line of maximum β stability and dotted lines show the N/Z ratio of the composite system for the respective systems. The direction and magnitude of the gradient of the potential-energy surface for the projectile-target system at contact is shown by dashed arrow. Data for ^{58}Ni and ^{64}Ni are from Ref. 4; data for ^{56}Fe are from Ref. 10.

ances, the neutron-proton correlation coefficients and the conditional variances.

Several factors may be responsible for the observed differences between the data and the transport model calculation. The diabatic dissipative dynamics model of Nörenberg² and the Schrödinger dynamical flow model of Griffin³⁶ provide two alternative approaches to the nucleon exchange model. Both stress mechanisms other than nucleon exchange in the early stages of the collision, which subsequently influence the evolution of the system in the direction of the experimental data. Moretto³⁷ and Schmidt³⁸ have suggested that the static and dynamic driving forces in damped collisions must be mediated by the necessity to equalize the temperatures of the two fragments as the system equilibrates. Thus, a feedback mechanism between nucleon transfer and temperature equilibration develops during the interaction time. This mechanism becomes particularly important in cases where the gradients in the potential energy surface are relatively weak.³⁹ This situation favors—on the average—the transfer of nucleons from the higher-temperature to the lower-temperature partner. For example, if excitation energy is equally shared in the initial states of nucleon exchange, the temperature $(E^*/A)^{1/2}$ of the lighter fragment (PLF) will be preferentially higher than that of the heavier fragment (TLF) due to the fragment mass asym-

metry. Hence, nucleon flow will be induced from the lighter to heavier subsystem in order to cool the system most efficiently.

In the early stages of the reaction the ratio of the total number of exchanges, $N_{\text{ex}} = \sigma_A^2$, to the net nucleon transfer from projectile to target, $N_{\text{net}} = A_p - A_{\text{PLF}}$, is relatively small, whereas as the damping increases, this ratio gradually increases, as shown in Fig. 12. Thus, initially a strong driving force exists for this feedback mechanism that favors the development of mass asymmetry between the fragments. As this force diminishes, the drift toward mass symmetry, as dictated by the potential energy surface, eventually dominates the mass flow. The possible importance of this relationship between net nucleon exchange and thermalization is further reinforced by studies of excitation-energy partition in damped collisions, which suggest a correlation between net nucleon exchange and heat transfer (see Refs. 10, 13, 15, 16, and 18).

Other possible considerations for the observed effects include the gradients of the potential-energy surface, which have a strong influence on the drift direction in the transport model. Since these gradients must be determined at each stage in the energy dissipation process, it may be necessary to incorporate the evolution of the PES as a function of interaction time in a more realistic way.

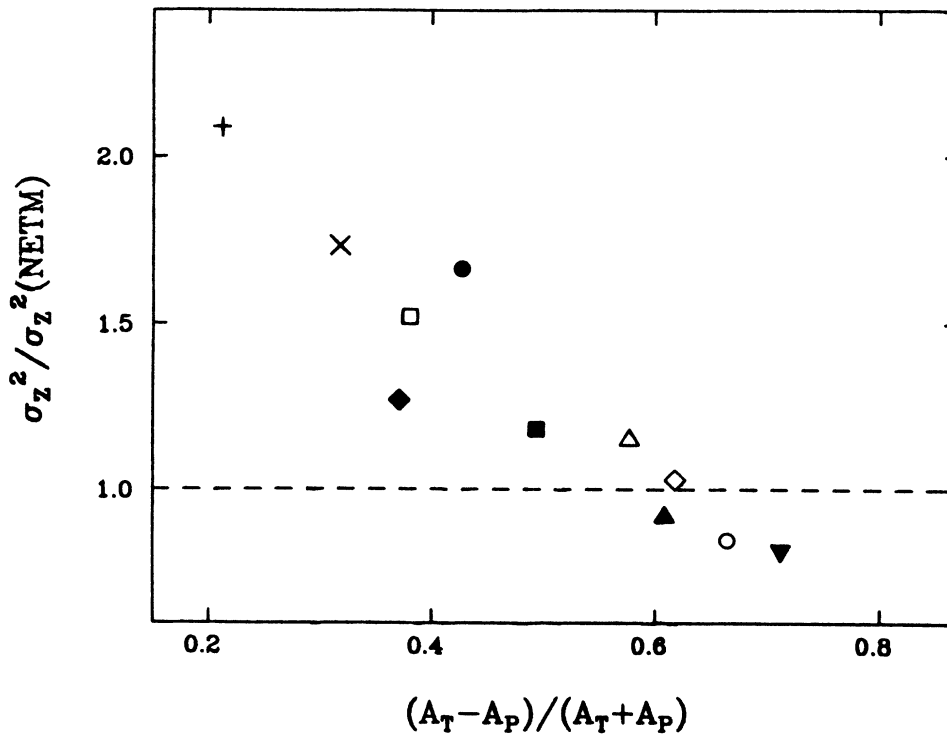


FIG. 11. The ratio of the experimental primary variances for proton exchange σ_z^2 , to the variances calculated with the nucleon exchange transport model at $E_{\text{loss}} = 100$ MeV. Data are plotted as a function of the target-projectile mass-asymmetry parameter $(A_T - A_P)/(A_T + A_P)$ for reactions with heavy target nuclei. For projectiles heavier than ^{74}Ge , we assume the primary and post-evaporative charge distributions are identical. Sources of data are: (\blacktriangle) ^{58}Ni and (\triangle) ^{64}Ni (Ref. 7); (\blacktriangledown) ^{40}Ca and (\circ) ^{48}Ca (Ref. 6); (\diamond) $^{56}\text{Fe} + ^{238}\text{U}$ (Ref. 4); and (\blacksquare) $^{56}\text{Fe} + ^{165}\text{Ho}$ (Ref. 4); (\blacklozenge) $^{56}\text{Fe} + ^{122}\text{Sn}$ (Ref. 5); (+) $^{136}\text{Xe} + ^{209}\text{Bi}$ (Ref. 33); (\times) $^{86}\text{Kr} + ^{166}\text{Er}$ (Ref. 34); and (\bullet) $^{84}\text{Kr} + ^{209}\text{Bi}$ (Ref. 35).

Such effects could be especially important if nonstatistical processes are important in the very early stages of damping, for example, giant resonances²⁸ or charge exchange.²⁹ Another possibility is that the neutron and proton mobilities used in the model may need adjustment. A lower mobility for neutron would improve the agreement with the centroid data; however, this would further lower the variances, which are already too low (Fig. 6).

Finally, the necking degree of freedom itself may need further refinement. For example, the larger variances for the $^{74}\text{Ge} + ^{165}\text{Ho}$ system relative to those for $^{56}\text{Fe} + ^{165}\text{Ho}$ may be due to a larger neck overlap region for the former case. This is suggested by the relationship between the ratios of experimental to calculated variances shown in Fig. 11. Here one observes that for relatively light projectiles, the model fits the data well. With increasing projectile size (i.e., greater overlap), the experimental variances significantly exceed the calculated values. If a significant neutron skin exists for ^{165}Ho , then the neck region that develops during the early stages of contact may be highly neutron rich. Because the surface neutron density for the ^{74}Ge projectile is considerably smaller than for the ^{165}Ho target, there will be a stronger isospin driving force for protons from the projectile to flow into this

region relative to proton flow in the reverse direction. Such a mechanism, which is not contained in the model, may provide an alternative means of explaining the charge drift toward asymmetry commonly observed in damped collisions.

V. SUMMARY

Both primary and post-evaporative fragment mass distributions have been measured for projectile-like fragments emitted in damped reactions between $E/A = 8.5$ MeV ^{74}Ge ions and ^{165}Ho . The results of this kinematic coincidence study permit a more microscopic examination of the nucleon exchange transport model, which has proven successful in accounting for many of the first-order features of damped collisions. The centroids of the distributions demonstrate a gradual evolution in the N/Z ratio of the PLF toward that of the composite system, although this value is never reached, even for fully damped events. The most striking conclusion to be drawn from this study is that the experimental and calculated centroids of the fragment nuclide distributions evolve in almost opposite directions. Experimentally, the direction of net nucleon drift favors transfer of the protons from

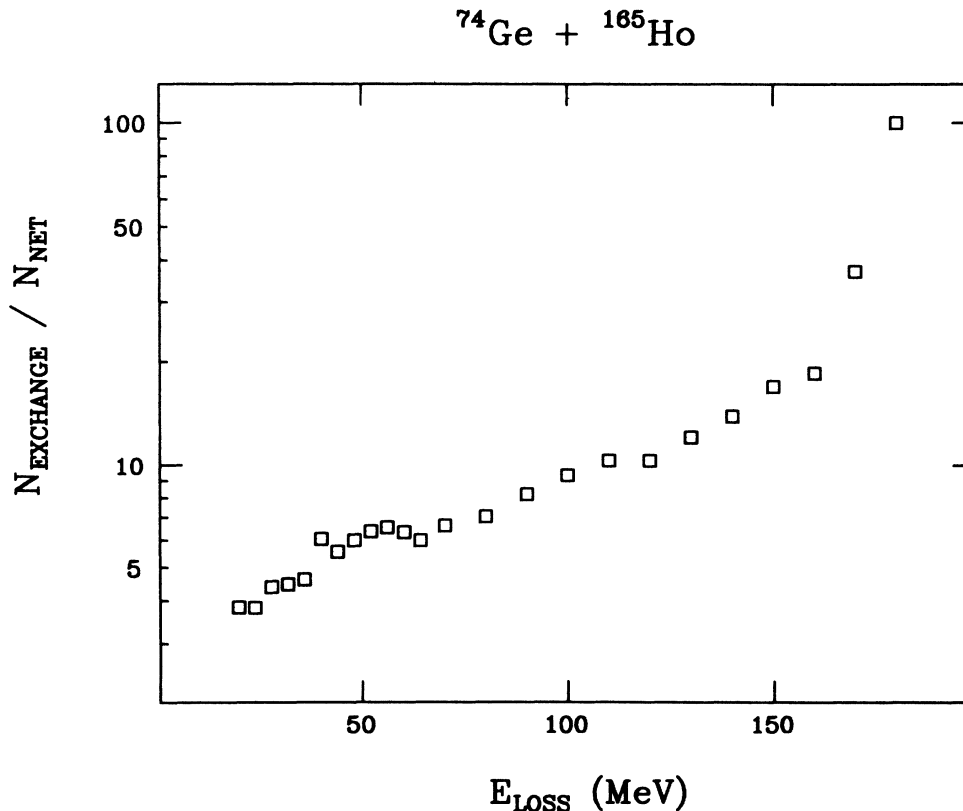


FIG. 12. Ratio of the total number of exchanges, $N_{\text{ex}} (\approx \sigma_A^2)$, to the net number of nucleon exchanges, N_{net} , as a function of energy loss.

the projectile to the target, whereas the net neutron drift is nearly zero. The net effect is a slight drift toward mass asymmetry. On the other hand, the nucleon exchange transport model predicts transfers to be dominated by neutron drift from target to projectile, with little net proton drift. The predicted net mass flow thus leads toward symmetry. Similar discrepancies between data and the calculations are observed for the variances, neutron-proton correlation coefficients and conditional variances of the distributions.

Comparison with other systems shows that the direction of net nucleon drift is roughly correlated with the gradient of the potential-energy surface at the injection point. The stronger the gradient, the stronger the correlation. Thus, it appears that nucleon exchange transport models require additional physics input in order to provide a more quantitative description of the experimental data. The concept of a feedback mechanism between nucleon exchange and thermalization offers one possible explanation of the observed deviations and provides the additional advantage of explaining the dependence of heat partition on net mass transfer. Details of the early stages

of the interaction and/or the subsequent influence of nucleon exchange on the potential energy surface should also be examined. Finally, the necking degree of freedom—both in terms of window-size and neutron/proton densities in the region—may require further investigation.

ACKNOWLEDGMENTS

The authors wish to express their thanks to J. Randrup for making available his transport code and for valuable discussions concerning this work. We also thank L. Tassan-got for providing us with results of his recent calculations. Harvey Syvesrud and the crew of the LBL SuperHILAC provided excellent beams during this experiment. We also acknowledge the assistance of Tom Gee for fabricating the targets, Bruce Rude and R.J. McDonald for assistance in setup of the scattering chamber, and Dick Yoder for assistance with the data reduction software. This work was supported by the U.S. Department of Energy and the National Science Foundation.

*Present address: Institute of Physics, Jagellonian University, Reymonta, 4, Kraków, Poland.

†Present address: Institute of Atomic Energy, Beijing, PRC.

¹J. Randrup, Nucl. Phys. **A307**, 319 (1978); **A327**, 490 (1979); **A383**, 468 (1982).

²W. Nörenberg, *New Vistas in Nuclear Physics* edited by P. J. Brussard and J. H. Koch (Plenum, New York, 1986), p. 81.

³H. Feldmeier, Rep. Prog. Phys. **50**, 1 (1987).

⁴H. Breuer, A. C. Mignerey, V. E. Viola, K. L. Wolf, J. R. Birkelund, D. Hilscher, J. R. Huizenga, W. U. Schröder, and W. W. Wilcke, Phys. Rev. C **28**, 1080 (1983).

⁵H. C. Britt, B. H. Erkkila, A. Gavron, Y. Patin, R. H. Stokes, M. P. Webb, P. R. Christensen, O. Hansen, S. Pontoppidan, F. Vidabeck, R. L. Ferguson, F. Plasil, G. R. Young, and J. Randrup, Phys. Rev. C **26**, 1999 (1982).

⁶R. De Souza, W. U. Schröder, J. R. Huizenga, R. Płaneta, S. H. Zhou, V. E. Viola, and H. Breuer, Phys. Rev. C **37**, 1783 (1988).

⁷R. Płaneta, S. H. Zhou, K. Kwiatkowski, W. G. Wilson, and V. E. Viola, Phys. Rev. C **38**, 195 (1988).

⁸H. Freiesleben and J. V. Kratz, Phys. Rep. **106**, 1 (1984).

⁹See, for example, W. U. Schröder and J. R. Huizenga, *Treatise on Heavy-Ion Science*, edited by D. A. Bromley (Plenum, New York, 1984), Vol. 2, p. 115.

¹⁰D. R. Benton, H. Breuer, F. Khazaie, K. Kwiatkowski, V. E. Viola, S. Bradley, A. C. Mignerey, A. P. Weston-Dawkes, and R. J. McDonald, Phys. Rev. C **38**, 1207 (1988); Phys. Lett. B **185**, 326 (1987).

¹¹T. C. Awes, R. L. Ferguson, R. Novotny, F. E. Obenshain, F. Plasil, S. Pontoppidan, V. Rauch, and G. R. Young, Phys. Rev. Lett. **52**, 251 (1984).

¹²R. Vandenbosch, A. Lazzarini, D. Leach, D.-K. Lock, A. Ray, and A. Seamster, Phys. Rev. Lett. **52**, 1964 (1984).

¹³H. Sohlbach, H. Freiesleben, P. Braun-Munzinger, W. F. W. Schneider, D. Schüll, B. Kohlmeyer, M. Marinescu, and F. Puhlhöfer, Phys. Lett. B **153**, 386 (1985).

¹⁴T. M. Semkow, D. G. Sarantites, K. Honkanen, Z. Li, M. Ross, J. R. Beene, M. L. Halbert, and D. C. Hensley, Phys. Rev. C **37**, 169 (1988).

¹⁵H. Keller, B. Bellwied, K. Lützenkirchen, J. V. Kratz, W. Bröchle, H. Gäggler, K. J. Moody, M. Schädel, and G. Wirth, Z. Phys. A **328**, 255 (1987).

¹⁶H. Gäggler, W. Bröchle, M. Brügger, M. Schädel, K. Sümmerer, G. Wirth, J. V. Kratz, M. Lerch, Th. Blaich, G. Herrmann, N. Hildebrand, N. Trautmann, D. Lee, K. J. Moody, K. E. Gregorich, R. B. Welch, G. T. Seaborg, D. C. Hoffman, W. R. Daniels, M. M. Fowler, and H. R. von Gunten, Phys. Rev. C **33**, 1983 (1986).

¹⁷D.-K. Lock, R. Vandenbosch, and J. Randrup, Phys. Rev. C **31**, 1268 (1985).

¹⁸K. Kwiatkowski, R. Płaneta, S. H. Zhou, V. E. Viola, H. Breuer, M. A. McMahan, and A. C. Mignerey, Phys. Rev. C **41**, 958 (1990), the following paper.

¹⁹K. Kwiatkowski, V. E. Viola, W. G. Wilson, S. H. Zhou, and H. Breuer, Nucl. Instrum. Methods **225**, 65 (1984).

²⁰H. Breuer, N. R. Yoder, A. C. Mignerey, V. E. Viola, K. Kwiatkowski, and K. L. Wolf, Nucl. Instrum. Methods **204**, 419 (1983).

²¹R. Bock, B. Fisher, A. Gobbi, K. Hildebrand, W. Kohl, U. Lynen, I. Rode, H. Stelzer, G. Auger, J. Galin, J. M. Lagrange, B. B. Back, and R. Albrecht, Nukleonika **22**, 529 (1977).

²²D. Hilscher, J. R. Birkelund, A. D. Hoover, W. U. Schröder, W. W. Wilcke, J. R. Huizenga, A. C. Mignerey, K. L. Wolf, H. Breuer, and V. E. Viola, Phys. Rev. C **20**, 576 (1979).

²³V. E. Viola, K. Kwiatkowski, and M. L. Walker, Phys. Rev. C **31**, 155 (1985).

²⁴A. Gavron, Phys. Rev. C **21**, 230 (1980).

²⁵V. E. Viola, A. C. Mignerey, H. Breuer, K. L. Wolf, B. G. Glagola, W. W. Wilcke, W. U. Schröder, J. R. Huizenga, D. Hilscher, and J. R. Birkelund, Phys. Rev. C **22**, 122 (1980).

²⁶K. E. Rehm, A. M. van den Berg, J. J. Kolata, D. G. Kovar, W. Kutschera, G. Rosner, G. S. F. Stephans, and J. L. Yntema, Phys. Rev. C **37**, 2629 (1988).

²⁷W. W. Wilcke, J. R. Birkelund, A. D. Hoover, J. R. Huizenga, W. U. Schröder, V. E. Viola, K. L. Wolf, and A. C. Mignerey, Phys. Rev. C **22**, 128 (1980).

²⁸R. A. Broglia, C. H. Dasso, and A. Winther, Phys. Lett. **53B**,

- 301 (1974); **61B**, 113 (1976).
- ²⁹H. Hoffman, C. Grégoire, R. Lucas, and C. Ngô, *Z. Phys. A* **293**, 229 (1979).
- ³⁰W. J. Myers and W. J. Swiatecki, *Ark. Phys.* **36**, 343 (1967).
- ³¹W. J. Swiatecki, *Prog. Nucl. Part. Phys.* **4**, 383 (1980).
- ³²L. Tassan-got, Ph.D. thesis, University of Paris Sud, 1989; L. Tassan-got and C. Stéphan, private communication.
- ³³W. U. Schröder, J. R. Birkelund, J. R. Huizenga, K. L. Wolf, and V. E. Viola, *Phys. Rep.* **45**, 301 (1978).
- ³⁴G. Rudolf, U. Lynen, A. Gobbi, A. Olmi, and H. Sann, *Nucl. Phys. A* **367**, 109 (1981).
- ³⁵J. R. Birkelund, H. Freiesleben, J. R. Huizenga, W. U. Schröder, W. W. Wilcke, K. L. Wolf, J. P. Unik, and V. E. Viola, *Phys. Rev. C* **26**, 1984 (1982).
- ³⁶J. J. Griffin and W. Broniowski, *Nucl. Phys. A* **428**, 145c (1984); J. J. Griffin, J. A. Lukasiak, and M. Dworzecka, *Z. Phys. A* **326**, 51 (1987).
- ³⁷L. G. Moretto and E. G. Lanza, *Nucl. Phys. A* **428**, 137c (1984).
- ³⁸R. Schmidt, *Nucl. Phys. A* **445**, 534 (1985).
- ³⁹J. Błocki, R. Płaneta, and K. Grotowski, *Proceedings of the XXIV Zakopane School on Nuclear Physics, Zakopane, 1989*, edited by J. Styczeń and Z. Stachura (World Scientific, Singapore, 1990).